Multi-scale dissolution dynamics for carbon sequestration in carbonate rock samples

Malin Haugen, Olav Parelius Folkvord, Torunn Veien, Martin A. Fernø, Bergit Brattekås [*]

Department of Physics and Technology, University of Bergen, Norway

ABSTRACT

Carbon dioxide (CO_2) sequestration in porous, sedimentary reservoirs is a key technology to mitigate emissions of anthropogenic CO_2 and curb irreversible climate change. The abundance of carbonate formations, both as saline aquifers and hydrocarbon reservoirs, makes future CO_2 storage in carbonate formations highly likely. The weak carbonic acid that forms when CO_2 dissolves in water will, however, interact with highly reactive carbonate. Preferential flow paths may form during dissolution or calcite precipitation may reduce injectivity - both processes significantly impacting reservoir sweep efficiency. Hence, understanding the dynamics of the dissolution processes and their influence on flow properties is necessary to safely store CO_2 in carbonate formations. Darcy and sub-Darcy scale dissolution kinetics were here assessed in carbonate core plugs with and without pre-existing highly permeable pathways, during multiphase flow and under relevant storage conditions.

Darcy-scale dissolution and precipitation data (injectivity changes, effluent analysis and mass loss) confirmed that CO_2 and brine co-injections altered the carbonate rock structure on Darcy scale, but could not determine the cause of change. Multi-modal imaging was applied to independently quantify structural changes with computed tomography (CT) and aqueous flow characteristics with positron emission tomography (PET), thereby determining injectivity dependence on local flow patterns. Formation of high permeability pathways, which was expected due to rock dissolution, was only observed in cores with pre-existing open fractures, where reactive flow was limited to the fracture plane. A good correlation between the two imaging modules was found: areas of higher porosity yielded a low-density CT signal (i.e. high number of voids present) and a high PET signal density (i.e. large volume of traced fluid present). Loss of injectivity suggested local changes in the flow pattern due to blocking of pore throats by moving particles or secondary precipitation or mineralization of dissolved ions. High-resolution PET imaging revealed cementation, that was also visible using micro-CT, hence determining sub-Darcy local flow obstructions that led to decreased Darcy scale injectivity. Multi-modal imaging, where core characteristics, such as large vugs and cementation, can be independently determined by complementary modalities, may therefore be a useful tool to quantify reactive flow and resulting dissolution in rock samples.

1. Introduction

Carbon capture and storage (CCS), where CO_2 is permanently stored in geological structures, has been identified as a proven technology to reduce carbon emissions to the atmosphere. The captured and injected CO_2 can be trapped in the reservoir by (mechanisms listed with increased storage security): structural or stratigraphic barriers (physical trapping); as immobile droplets (residual trapping); dissolved in the aqueous phase (solubility trapping); and as a solid part of precipitates (mineral trapping) (IPCC, 2005). Geological storage sites for CO_2 injection include depleted oil and gas reservoirs and saline aquifers, both in sandstone and carbonate formations (IPCC, 2005). Injection of CO_2 for enhanced oil recovery (CO_2-EOR) has been widely implemented in both sandstone and carbonate since the 1970s (Laboratory, 2010). CO_2-EOR with simultaneous storage of CO_2 in the reservoir may be an important contributor to fast upscaling of carbon sequestration (Alcorn et al., 2022). Saline aquifer storage has mostly targeted sandstone formations; however, to achieve ambitious emission goals, utilization of the vast storage capacity in carbonate formations is also necessary.

Carbonate is a class of highly reactive sedimentary rocks mainly consi

sting of carbonate minerals, where the two major types are limestone and dolomite. Limestone, used in this study, mainly consists of different crystal forms of calcium carbonate ($CaCO_3$), with carbonate formation brines often containing NaCl, $CaCl_2$ and $MgCl_2$ (Oelkers et al., 2008). The combination of chemical components in rock and fluids makes carbonates susceptible to structural changes, where both dissolution and re-precipitation of carbonate minerals may occur during CO_2 injection for geological sequestration (Benson and Cole, 2008). Dissolution and development of highly conductive (wormholes) or blocked pathways have implications for large-scale deployment of CCS in carbonates. Wormholes can increase near-well injectivity, but a network of connecting wormholes can cause conformance issues between wells that reduce sweep efficiency and CO_2 storage potential (Larkin and Creel,

2008; Smith et al., 2006).

Dissolution mainly occurs when injected CO2 dissolves in the aqueous phase, develops carbonic acid and reduces the aqueous phase pH. At neutral to alkaline pH, mineral trapping is expected to occur by the formation of carbonate minerals from the available cations in the present brine [8, 9]. Minto et al. (2017) reported several possible mechanisms for re-precipitation, including: 1) occurrence of supersaturated fluid due to mixing with higher pH water trapped in stagnant pores, and 2) decrease in $CaCO_3$ solubility due to pressure reduction as fluids are transported through a porous medium. Depending on the flow conditions, precipitated minerals (fines) can either remain in place or be transported with the flowing fluids. Minerals may re-precipitate when flowing through a porous medium; consequently blocking pores or preferential flow paths.

1.1. A short summary of experimental work on the Darcy scale

Darcy scale investigations are necessary to investigate flow implications from carbonate dissolution. In addition to being reactive, carbonates are often heterogeneous with a high porosity, low matrix permeability and natural fractures. Carbonate core samples can be homogenous or heterogeneous, and fluid transport during and after dissolution and re-precipitation is strongly influenced by local rock structure. Several authors have experimentally verified the dependence of dissolution on core structure; e.g. in (Al-Khulaifi et al., 2019; Maheshwari et al., 2013) where uniform dissolution was observed in homogeneous limestone, while wormholes formed in more heterogeneous samples. Highly conductive wormholes were also observed in vuggy limestone during carbonated brine injection, while uniform dissolution was observed in relatively homogenous marly dolostones (Hommel et al., 2018; Smith et al., 2013). Luhmann et al. (2014) used x-ray computed tomography (CT) to visualize carbonated brine injection in dolomite core plugs at reservoir conditions (100 °C and 150 bars) and found that dissolution patterns were rate-dependent: conductive wormholes at high (47 cm/h) injection rate, narrow wormholes at intermediate (5 cm/h) rates, and cone-shaped dissolution at low (0.5 cm/h) injection rates.

Single-phase reactive transport (carbonated brine as the only flowing phase) occurs far from the injection well, where CO_2 and brine in equilibrium forms a single phase. The injected CO_2 and formation brine (with and without CO_2 saturation) may co-exist closer to the well during CO_2 injection. Single-phase and two-phase reactive dissolution experiments performed in Estaillades limestone (Ott et al., 2015) resulted in wormhole formation during single-phase injection (injection rate 1 cm/h) and compact dissolution during co-injection (injection rate 120 cm/h, but equal Damkohler and Péclet numbers to single-phase injections). Compact dissolution was explained by capillary forces, causing CO_2 to preferentially occupy small wormholes forming at the inlet end of the core plug (Ott et al., 2015). Free CO_2 is not reactive, hence preventing further growth of the wormholes. Luquot and Gouze (Luquot et al., 2009) pre-mixed and injected different fractions of CO_2 and brine into limestone core plugs at a temperature of 100 °C and a system pressure of 120 bar. Four flow experiments were conducted, where the CO_2 fractions varied between 6 and 83%. Injection rates ranged between 108 ml/h (high CO_2 fraction) to 57 cm/h (low CO_2 fraction), and the results indicated that uniform dissolution occurred at low CO_2 fractions and wormholes at higher CO_2 fractions.

The experimental efforts in this paper focus on the relationship between carbonate dissolution and Darcy-scale structural changes. First, CO_2 and brine were co-injected in whole (un-fractured) limestone cores and structural changes and implications for flow were analyzed. Second, CO_2 and brine were co-injected in the same core material with added heterogeneity (fractures). Two fracture systems were studied: *open fracture cores* (longitudinal fracture with large, irregular aperture mimicking a pre-existing wormhole) and *tight fracture cores* (longitudinal fracture with small and uniform fracture aperture). The different

dissolution regimes were analyzed based on global measurements, and in some cores *in-situ* visualization was utilized for improved understanding. High-resolution imaging encompassing both structure (micro-CT) and flow (micro-PET) gave access to sub-core dissolution and secondary precipitation regimes.

2. Methods and materials

2.1. Fluids

Fluid properties used during the experiments are listed in Table 1. The CO_2 fraction used during co-injections was 80%, representative of the near wellbore area where the aquifer is saturated with CO_2 with the presence of a free CO_2 phase. A previous study found that a CO_2 fraction of 80% resulted in the formation of highly conductive flow channels and 20% CO_2 in uniform dissolution (Luquot et al., 2009)..

2.2. Carbonate core samples

Cylindrical Edwards limestone core plugs were drilled from larger blocks, gently washed with distilled water and dried at 60 °C for two weeks. The Early Cretaceous carbonate rocks were sourced from West Texas. Previous work characterized the Edwards limestone core material, and reported a trimodal pore size distribution containing microporosity and vugs (Fernø et al., 2015). The carbonate rock is mainly composed of calcium carbonate mineral ($CaCO_3$) and is highly reactive. Both whole (five cores) and fractured systems (five cores) were studied (see Table 2). A Brazilian test fracturing procedure (Brattekås et al., 2020) was used to create different fracture types: *open fractures* (longitudinal fracture with large, irregular aperture) and *tight fractures* (longitudinal fracture with narrow and uniform fracture aperture). The fracturing procedure creates natural fractures with significant local heterogeneity. The Brazilian test blade determined the fracture type (Brattekås et al., 2020), where L1T, L2T and L3T were classified as *open* and L4T and L5T as *tight*. Visual inspections of the core exterior and mass loss during fracturing (1 g of rock particles removed from the core during fracturing for open fractures, 0.5 g for tight) confirmed the fracture type (Figure A5). Matrix permeabilities were in the range of 20–50 mD for the cores used in this study. Initial fracture conductivity varied significantly within the open fracture cores due to local heterogeneities (Table 2). Variations were also observed in tight fractures, mainly due to additional measures taken in core L5T to promote flow in the fracture interior (silicon strips were mounted along the core to close fracture edges).

2.3. Experimental set-up and procedure

The cores were saturated with brine (Table 1) under vacuum, and porosity (Table 2) was determined gravimetrically. Absolute permeability (Table 2) was measured during single-phase injection of the same brine at different volumetric rates and calculated using Darcy's law, where the entire core cross-section was used as basis for calculation in both whole and fractured cores. Note that the injected brine mainly channels through the fracture in cores L1T - L5T (i.e. the cross-sectional area conducting flow which will vary between fracture types and locally within cores). Initial fracture conductivities (Table 2) are therefore more uncertain, but nevertheless provided to indicate whether flow occurs mainly in the fracture network (initial fracture conductivity » matrix permeability range) or is likely more evenly distributed in the core (initial fracture conductivity ≈ matrix permeability range). Each core plug was wrapped in aluminum foil to minimize exposure between CO_2 and the Viton rubber sleeve and mounted in a Hassler-type core holder connected to the flow system (Fig. 1). A confinement pressure of 92–105 Bar (12 bars above pore pressure) was maintained during all injections. The injected mixture during co-injections (80% CO_2 and 20% brine volumetric fractions) was flooded through the bypass, and pH was

Table 1

Fluids used in core flooding experiments. The brine composition was representative of a generic carbonate formation brine.

Fluid	Content	Density [g/ml]	Viscosity [cP]	pH
Brine	Distilled water with 4.0 wt% NaCl	1.05 (20 °C, 1 bar)[1]	1.09 (20 °C, 1 bar)[a]	5.58
	3.4 wt% CaCl$_2$	1.05 (40 °C, 90 bar)	0.65 (40 °C, 90 bar)	
	0.5 wt% MgCl$_2$			
	0.01 wt% NaN$_3$			
CO$_2$	>99.99% pure CO$_2$	0.49 (40 °C, 90 bar)[b]	0.03 (40 °C, 90 bar)[b]	–
Co-injection	Brine with 80% CO$_2$			4.28*

* Measured at ambient pressure, after the back pressure regulator (Fig. 1).
[a] Values from (Fernø et al., 2015).
[b] Values from (Lemmon et al., 2020).
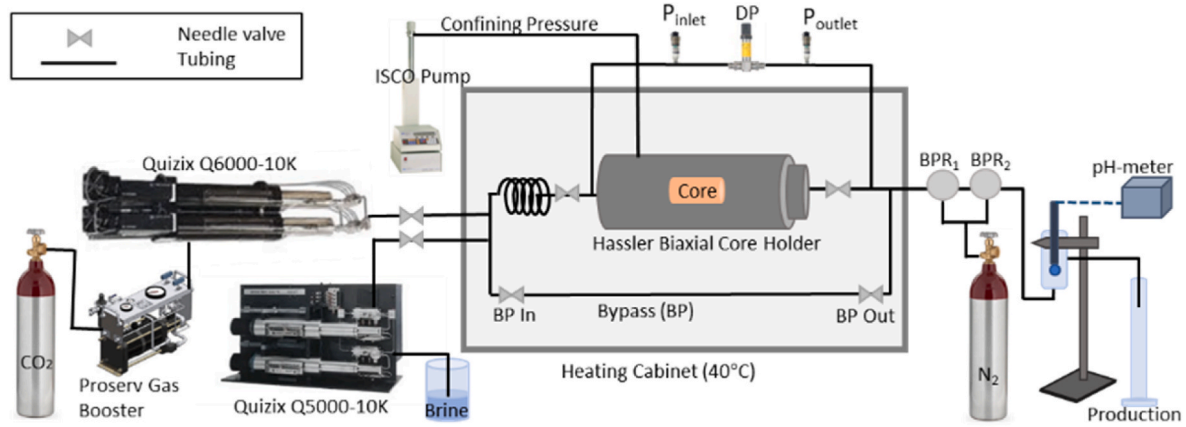
Fig. 1. Laboratory setup used during dissolution experiment. The Hassler biaxial core holder was mounted in a heating cabinet, and connected to a 10 m long coil upstream of the core inlet to ensure that injected fluids reached elevated temperature conditions prior to entering the core. The fracture plane was kept horizontal during co-injection to minimize gravitational effects. Temperature was kept constant at 40 °C. Quizix plunger pumps Q5000-10k and Q6000-10k were used for brine and CO$_2$ injections respectively, and an ISCO pump for confinement pressure. Absolute (ESI 0–400 bar) and differential pressure transducers (Aplisens 0–16 bar for whole cores and 0–2.5 bars for fractured cores) were used to monitor dynamic pressure developments during injections. Two back pressure regulators (Equilibar) maintained and stabilized the pore and system pressures. The inline pH meter (Ati q45p) measured effluent pH at ambient conditions.

Table 2

*Measured core properties including dimensions, porosity, absolute permeability. * For fractured cores (L1T – L5T) $K_{w,initial}$ indicates the initial fracture conductivity. In core L5T a silicon strip was mounted longitudinally along the core to limit flow along the edges of the fracture.*

	Core ID	Length [cm] ±0.01	Diameter [cm] ±0.01	Porosity [%] ±0.05	$K_{w,initial}$ [mD] ±0.5
WHOLE	L2	7.33	3.80	22.2	48.1
	L3	7.00	3.78	27.1	78.0
	L4	7.26	3.79	21.4	21.8
	L7	7.64	3.80	21.9	31.5
	L8	7.04	3.80	23.2	43.4
FRACTURED	L1T	7.31	3.78	22.3	387*
	L2T	7.33	3.78	24.6	605*
	L3T	7.00	3.78	24.0	649*
	L4T	6.96	3.78	26.7	463*
	L5T	6.78	3.78	22.6	38*

measured at ambient conditions with an inline pH meter (*Ati q45p*) before flooding through the core. The produced effluent pH was also measured during co-injection (for fractured cores only). The differential pressure was continuously monitored (*Aplisens differential pressure* 0–16 bars, and ESI absolute pressure 0–400 bars) to assess core dissolution and the dynamic formation of preferred flow paths. The injectivity index J_{index} was used to monitor injectivity development during co-injection and is given by:

$$J_{index} = \frac{Q\left[\frac{ml}{h}\right]}{dP\,[bars]} \qquad (1)$$

where Q is the volumetric flow rate though the core plug and dP is the pressure drop across the core plug. Minor pressure fluctuation is expected in this system due to rapid changes in local saturations and relative permeability (not accounted for in global measurements). The injectivity index was used to evaluate changes in flow potential over time. After injection of the desired pore volumes (PV inj, Table 3), CO$_2$ injection was stopped while brine injection continued for 24 h to displace CO$_2$ from the pore network and measure post-dissolution absolute permeability. The relation between pre- and post-dissolution absolute permeabilities, is given by the impedance factor:

$$J = \frac{K_0}{K} \qquad (2)$$

where J is the impedance factor, Ko the absolute permeability of the core after dissolution, and K the initial permeability of the core. The cores were visually inspected after removal from the core holder and photographed (images may be found in the supplementary material, Figure A.5 and Figure A.6). The produced effluent was filtered (0.45 µm Supor filter) and the debris was analyzed with X-Ray Diffraction (*D8 ADVANCE ECO XRD*) to shed light on the crystalline phases present (only for cores L2T, L3T and L4)

Spatially resolved dissolution cannot be quantified by global measurements; a selection of cores (Table 3) were therefore imaged using high resolution µCT and µPET. µCT (ProCon X-ray CT-ALPHA) was used both pre- and post-dissolution to visualize and quantify structural changes caused by dissolution. The µCT images were obtained at no-flow static conditions and enabled micrometer scale investigation of dissolution patterns, vugs, cementation and visible wormholes. The µ-CT scanner used a 125 kV micro-focus tube with a 3000 x 3000 pixel

Table 3

Overview of flow parameters. The Darcy velocity is calculated using the whole core cross-section, hence the actual Darcy velocity in fractured cores is likely higher than reported.

	Core ID	P_{pore} [barg]	Q [ml/h]	Q_{Darcy} [cm/h]	PV inj	Fracture system	Imaging module Pre/post dissolution
WHOLE	L2	92	36	3.2	400	n.a.	µCT/µPET
	L3	93	72	6.4	400	n.a.	-/µPET
	L4	93	24	2.1	400	n.a.	-/µCT + µPET
	L7	80	48	4.3	392	n.a.	-/µPET
	L8	90	60	5.3	400	n.a.	-/-
FRACTURED	L1T	80	20,40,80,160	1.8–14.3	392	Open	µCT/µCT + µPET
	L2T	90	40	3.6	216	Open	µCT/-
	L3T	90	80	7.1	406	Open	µCT/µCT + µPET + PET
	L4T	90	80	7.1	368	Tight	µCT/-
	L5T	90	40	3.6	222	Tight	µCT/µCT

detector, and scanned each core with a continuous helix motion using 1600 projections for each rotation. The exposure time was set to 500ms, and the reconstructed images had a spatial resolution of 29.2 µm. Micro-Positron Emission Tomography (µPET) imaging was used to visualize flow in partly dissolved core plugs after co-injection using a traceable [18]FDG-brine (experimental setup and general procedure detailed in (Brattekås et al., 2023)). µPET imaging was performed during miscible brine-[18]FDG-brine injections using the same total volumetric rate and core orientation as during co-injection. Reconstructed images had spatial and temporal resolutions of 0.42 mm (voxel size) and 60 s.

3. Results and discussion

This section presents multi-scale (Darcy and sub-Darcy) experimental results and analysis during and after co-injections, describing the temporal changes in injectivity index, impedance factor and pH, in addition to changes in rock structure (µCT) and flow paths (µPET) from the carbonate dissolution and precipitation processes (cf. Table 4).

3.1. Darcy-scale investigations

Darcy-scale measurements include pH and differential pressure measurements (dynamic during co-injection) and visual inspection of the core exterior and effluent analysis (after co-injection).

3.1.1. Injectivity and impedance development during co-injection

The injectivity index (Eq. (1)) was monitored during co-injection of supercritical CO_2 and brine (operational parameters in Table 4) for whole and fractured cores (see Fig. 2). The injectivity index behavior falls into two categories: *increasing* and *decreasing*. In open fracture cores (L1T, L2T and L3T) injectivity *increased* over time (injectivity index >1.0 relative to initial value, cf. Table 4), due to localized dissolution in the fracture plane, efficiently increasing the fracture aperture. In whole (L3 and L4) and tight fracture cores (L4T and L5T) injectivity *decreased* over time (injectivity index <1.0 relative to initial value, cf. Table 4), caused

by dynamics in dissolution and precipitation mechanisms that were more pronounced within porous media and narrow fractures (further discussed in 3.2). Pressure fluctuations were observed throughout co-injection for all cores, as expected during two-phase flow, but with less fluctuations in open fracture cores compared to whole and tight fractures (the reader is referred to Figure A.1 and A.2 for all results).

The development in effluent pH during co-injection of supercritical CO_2 and brine (see Fig. 3) describes the Darcy-scale dissolution of $CaCO_3$ that leads to formation of bicarbonate ions (HCO_3^-) which re-increase the aqueous phase pH (Minto et al., 2017; Gaus, 2010). The pH development in fractured systems indicated an effect of initial fracture conductivity. In open fracture cores (L2T and L3T) the effluent pH relative to the injected phase increased before 1 PV injected, compared with tight fractures cores (L4T and L5T) where a pH increase was not observed until 3.5 PV injected. The effluent pH remained above the injected pH after gas breakthrough, indicating sustained (continuous) dissolution throughout co-injection.

Two further observations confirmed dissolution of core material in all studied systems: 1) calcite minerals (confirmed with XRD, see Figure A4) were observed in the effluent after gas breakthrough, and 2) up to 2.1% mass loss (cf. Table 4) was recorded post-dissolution for whole cores. Visual external inspection post co-injection (Figure A5 and A.6) also supported dissolution: *whole cores* were predominately dissolved at both end faces, cores with *tight fractures* were dissolved at the inlet face (less at outlet), whereas cores with *open fractures* showed dissolution along the pre-existing fracture plane.

Darcy-scale dissolution and precipitation data (injectivity, impedance, XRD, pH, weight and core exterior investigation) confirmed that CO_2 and brine co-injections altered the rock structure of all cores. Dissolution and the associated formation of high permeability pathways (wormholes) were expected to increase injectivity in all cores. Nevertheless, the injectivity increased only for open fracture cores, where the pre-existing conductive fracture plane concentrated reactive fluid flow in a limited area. The recorded mass loss confirmed that dissolution also occurred in whole cores, but the loss of injectivity suggests that

Table 4

Darcy velocity, injectivity, permeability, impedance and mass loss for studied systems during co-injections. End point weight was not recorded for fractured cores (i.e. mass loss not provided).

|	Core ID	Darcy velocity [cm/h]	Injectivity index @ 200 PV (relative to start)	$K_{w, inital}$ [mD] ± 0.5	$K_{w,post\ dissolution}$ [mD]	Impedance factor	Mass loss [%]
WHOLE	L2	3.2	163 (0.4)	48.1	20	2.4	0.6
	L3	6.4	307 (0.5)	78.0	38	2.0	1.9
	L4	2.1	97 (0.5)	21.8	15	1.5	2.1
	L7	4.3	169 (0.7)	31.5	19	1.7	0.6
	L8	5.3	147 (0.7)	43.4	21	2.1	0.9
FRACTURED	L1T	1.8–14.3	2245 (8.2)	387	1370	0.3	n.a
	L2T	3.6	3863 (6.8)	605	716	0.8	n.a
	L3T	7.1	2944 (3.4)	649	655	1.0	n.a
	L4T	7.1	350 (0.7)	463	36	12.8	n.a
	L5T	3.6	275 (0.8)	38	26	1.5	n.a
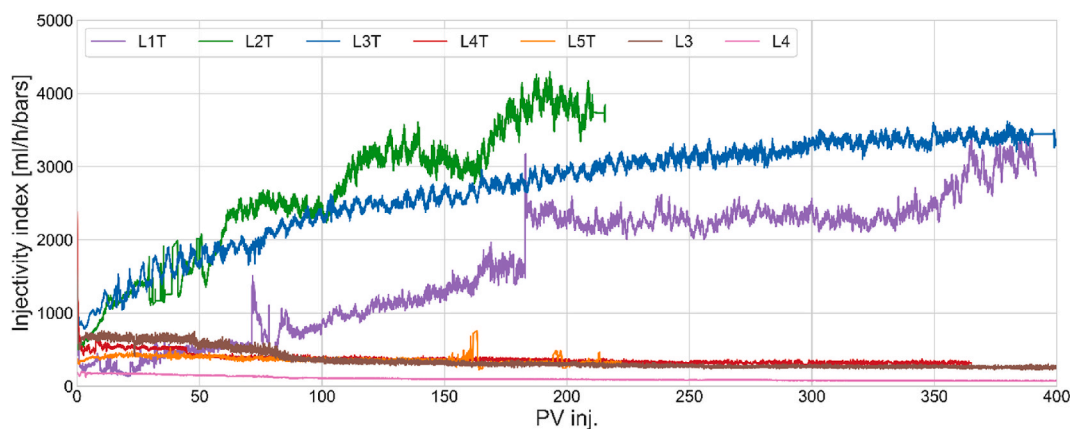
Fig. 2. Development in injectivity index for whole cores (L3 and L4), cores with tight fractures (L4T and L5T) and cores with open fractures (L1T, L2T and L3T) during co-injection of supercritical CO_2 and brine. An increasing injectivity was only observed in cores with open fractures, although dissolution occurred in all cores. Differential pressures fluctuated for all cores (detailed plot included in the supplementary material (Figure A.1)).
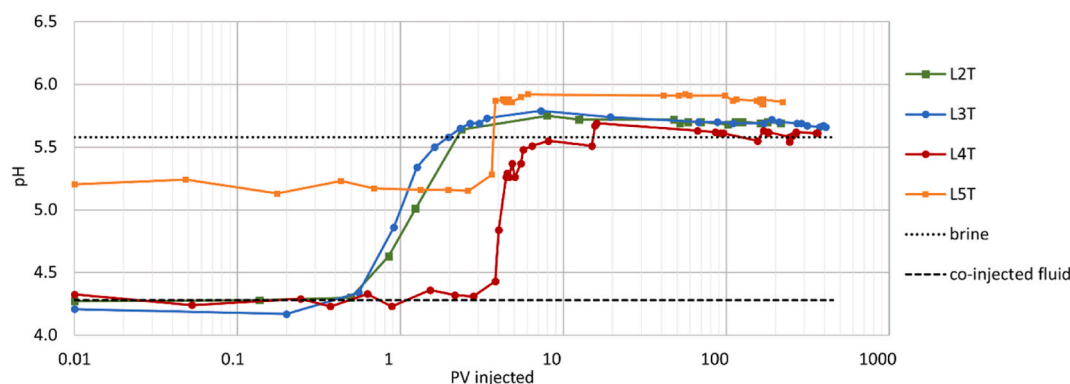

Fig. 3. Development in effluent pH during co-injection in fractured cores. The open fracture cores (L2T and L3T, pH was not measured in L1T) show a pH increase before 1 PV injected, compared with tight fracture cores (L4T and L5T) both with increased pH after 3.5 PV injected. The injected brine pH (grey dotted line) was 5.58 and the pH of co-injected fluid (20% brine and 80% CO_2; dashed black line) was 4.28. Note: The pH value for L5T prior to breakthrough was higher than the co-injected fluid due to contaminated outlet tubing: it is expected that the pH should be comparable to co-injected fluid before breakthrough. Also note the logarithmic x-axis. Differential pressure related to measured pH is presented in Figure A3.
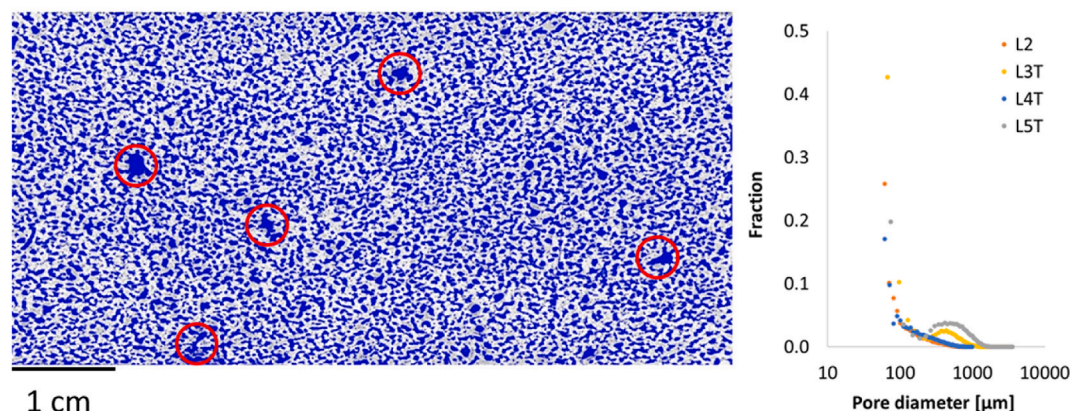

Fig. 4. Spatially resolved pore size distribution from µCT image (left, core L2), where blue represents the pores above the lower image resolution limit (31 $\pm$ 2 µm) with large pores (vugs) indicated in red circles. Distribution of pore diameters (µm) for four cores (right) show some variation, but also demonstrated that the majority of pores were small (20–40% of pores were close to the resolution limit for all cores), with few pores above 100 µm. Analysis is based on equal volumes in the interior of each core (2.5*2.5*5 cm in the x, y, z directions, respectively) to avoid beam hardening and end effects.

secondary precipitation may have occurred due to oversaturation and change in solubility. The decreased injectivity observed in whole and tight fracture cores may, therefore, be explained by 1) re-arrangement of partly dissolved calcite crystals blocking narrow pore-throats downstream, and/or 2) secondary precipitation or mineralization of dissolved ions, both of which may cause local changes in the flow pattern. Note the difference between tight fracture cores L4T and L5T: in L5T fluid flow along fracture edges was physically limited and initial
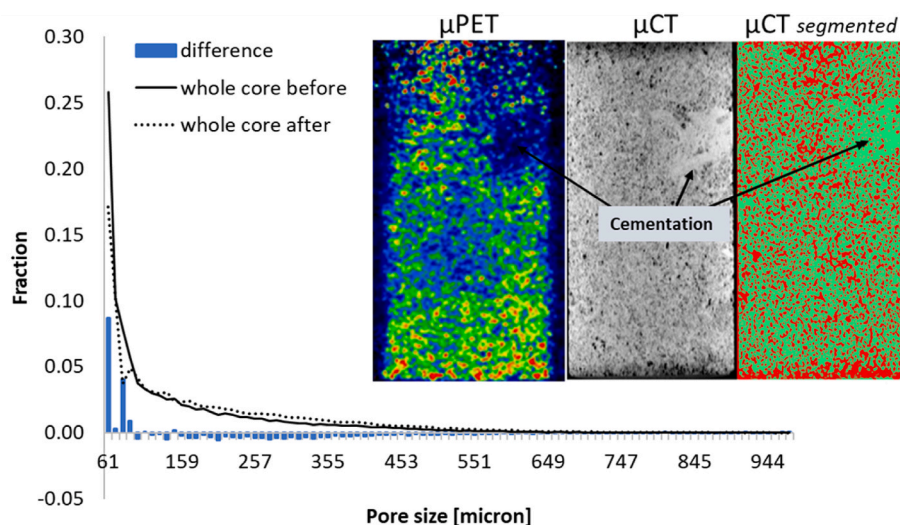
Fig. 5. Quantitative comparison of pore size distribution before (core L2) and after co-injection (core L4) and sub-Darcy multi-modal visualization (inset, core L4). The pore size distributions were obtained for the core interior (2 x 2 × 6.5 cm) to avoid artifacts from beam hardening and end effects. The difference (blue columns) between pore sizes before and after co-injection shows a loss of small pores (60–90 μm) and a gain in medium and larger pores (negative difference values). Hence, the dissolution and precipitation processes may have increased the size of some pores while clogging smaller pores by fines during transport. A 32% reduction in observable pores was found after co-injection. A similar trend was observed in whole core L3 (not included here). Inset: multi-modal imaging of water distribution (μPET) and rock structure (μCT) in the XZ plane. A cemented, low-porosity (2%, calculated from μPET) region with low water content (dark blue region, 'μPET' image) and high-density (bright, 'μCT' image) rock matrix was observed. Pore sizes were below image resolution (red pores and green matrix, 'segmented μCT' image). The water saturation was generally higher (warmer colors) in the inlet region compared with the outlet region, attributed to Darcy-scale dissolution heterogeneity. Porosity profiles for L3 and L4 are added to the supplementary material (Figure B1 and B.2 respectively) and show both cementation (L4) and dissolution (L3). Cores L2 and L7 did not exhibit structural changes quantifiable by μPET.

fracture conductivity, hence, significantly lowered compared to L4T. Post dissolution permeabilities are, however, comparable in the two cores, which supports that local particle re-arrangement and/or precipitation occurred in the fracture network: with fluid diversion into the core interior as a direct consequence for L4T. Determining where dissolution and/or clogging occurred within the core pore space is not possible from global Darcy-scale measurements.

3.2. Sub-Darcy scale investigation

To better understand where the carbonate reactive processes occurred within the core plugs, and how flow was influenced, *in-situ* imaging was applied after co-injection. The analysis was performed in fully brine-saturated conditions, under the assumption of static conditions with all reactive processes at equilibrium.

3.2.1. Pore size distribution

The rock material has trimodal distribution of pore sizes, with comparable size distribution for all studied core samples (see Fig. 4). The majority (80%) of pores were smaller than 200 μm, with most pores present close to the resolution limit. Sub-Darcy image analysis demonstrated a minority of vugs (larger pores; 2400–3000 μm), corroborating previous thin-section analysis (Tipura, 2008).

3.2.1.1. Local changes in pore space and flow. The effect of local rock structure changes on flow (see Fig. 5) may be studied with multi-modal imaging by comparing spatially resolved rock density (μCT images) with water distributions (μPET images). Whole cores where impedance factors increased during co-injection (>1, see Table 4) generally demonstrated a nonuniform porosity distribution after co-injection, where local regions of low porosity relative to surrounding rock matrix were prominent. A low-porosity region (i.e. region with high rock density) aligned with reduced water flow (i.e. low permeability) in core L4 (Fig. 5). Higher-porosity regions coincided with a preferential flow path of injected water post dissolution.

A quantitative comparison of pore size distribution before and after

co-injection was used to inform the discussion of rock structural changes as a result of carbonate dissolution and precipitation processes (see Fig. 5). The quantitative analysis suggests that the core was partially clogged by calcite particles from dissolution downstream, leading to local areas with cementation. Note that cementation was not observed for any core prior to co-injection. Visible exterior changes (cf. Figure A6) were not seen at the outlet of this core; and the impedance factor was 1.5 (i.e. a 50% decrease in absolute permeability). Sub-Darcy structure changes after co-injection was resolved with μPET by evaluating the dynamics of a miscible water-water displacement.

#### 3.2.2. Relationship between impedance factor and local dissolution

The fractured cores fall into two impedance-based categories: *increased* (>1.0, cores L5T and L4T) and *decreased* (≤1.0, L1T, L2T and L3T).

The decreased impedance factor observed in cores with open fractures (L1T, L2T and L3T) implied geometric changes in the pre-existing fracture plane, exemplified below for core L1T with the lowest (0.3) impedance factor (see Fig. 6). Post-dissolution visualization with multiple imaging modalities confirmed that dissolution occurred, with an average porosity increase of 13% in the fracture plane compared to 5.5% in the rock matrix (quantified by μCT). Although dissolution had occurred in most of the pore space, flow occurred exclusively in the fracture plane post-dissolution (quantified by μPET). Hence, the open fracture cores retained reactive flow in the irregular fracture aperture (mimicking a pre-existing wormhole), causing further local dissolution in the main flow path.

A different dissolution-impedance factor relationship was observed for open fracture core L3T, where an increase in porosity was also measured both in and around the fracture plane. The porosity change (by dissolution) was largest in the fracture area close to the inlet (first 3 cm core length) compared with the middle and outlet (see Fig. 7). In contrast to fractured core L1T (impedance factor 0.3), the impedance factor for core L3T was 1 (i.e., no change in Darcy scale permeability before and after dissolution), see Table 4. Local flow analysis showed that flow occurred both inside and outside of the pre-existing fracture
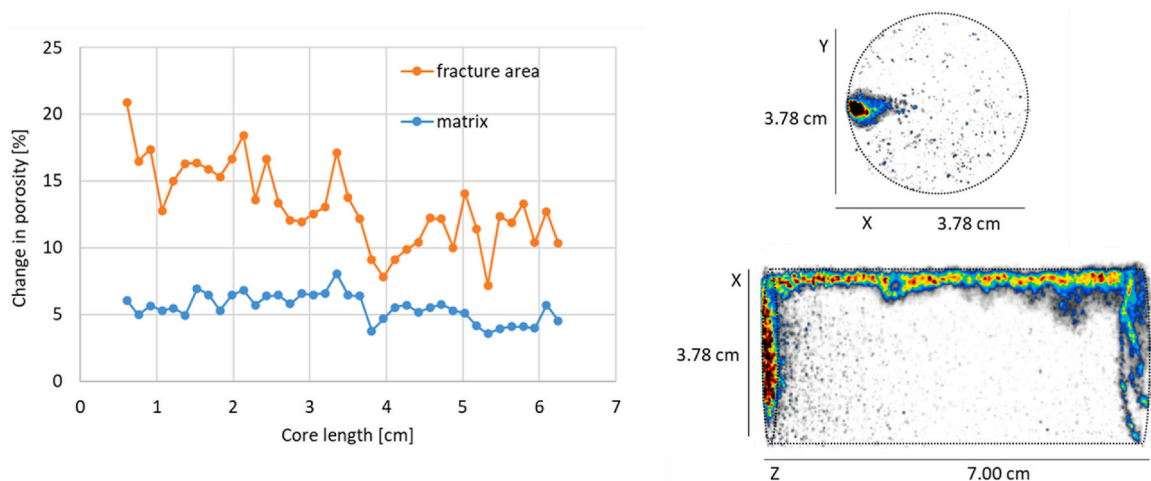
Fig. 6. Profiles of porosity change (left) and the localized fracture plane flow (right) after co-injection in open fracture core L1T. Left: The porosity increased both in the fracture region (orange, on average 13.2%) and in the rock matrix (blue, on average 5.5%). Hence, most of the dissolution occurred in the fracture plane, leading to increasing injectivity and reduced impedance. The porosity profiles are calculated by quantitative comparison of three-dimensional μCT images before and after co-injection. Right: The accumulated μPET signal (XY- and XZ plane) shows that the open, longitudinal fracture was the dominating flow conduit, with some dissolved regions near the inlet and outlet end faces. Warmer colors indicate more brine present. Note: for the porosity profiles the spatial resolution was XY-plane = 60 μm (two pixels) and slice thickness of Z = 1.5 mm. Five slices were omitted at the inlet and outlet to reduce the influence of end effects.
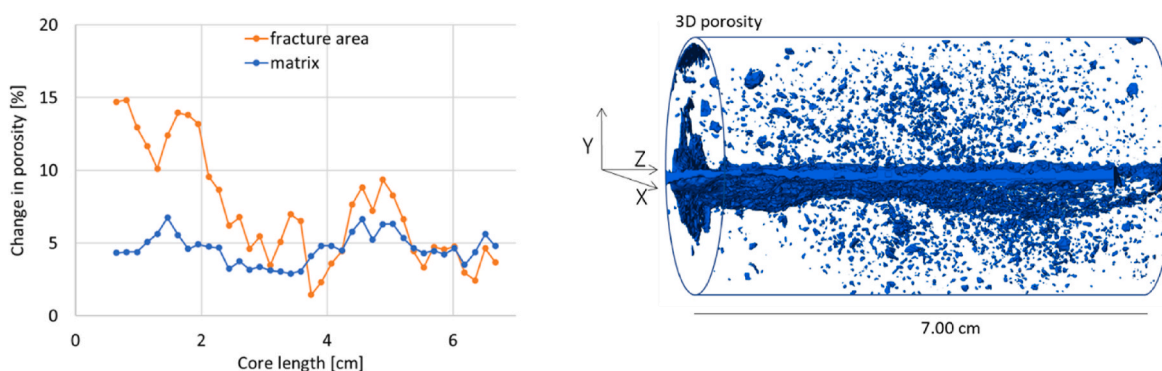
Fig. 7. Quantitative porosity change profiles and 3D resolved porosity change after co-injection in open fracture core L3T. Left: Porosity changes by dissolution in the fracture area (orange) and matrix (blue) after co-injection, visible by μCT. Dissolution in the fracture area was on average 7%, with more pronounced porosity change close to the inlet (0–3 cm). In the core middle and outlet (3–7 cm) both matrix and fracture porosity averaged 5%. Regions where the matrix porosity change exceeded the fracture area suggest that more dissolution occurred outside of the fracture plane. Right: Visualization of spatially resolved void (>50 μm, blue) calculated from μCT images show that dissolution occurred in the majority of the core, not only in the pre-existing fracture plane. (Additional micro-CT images available in supplementary material, Figure B3). Note: for the porosity profiles the spatial resolution was XY-plane = 60 μm (two pixels) and slice thickness of Z = 1.5 mm. Five slices were omitted at the inlet and outlet to reduce the influence of end effects.

plane post-dissolution (quantified by μPET). Hence, the anticipated reactive flow discrimination to the pre-existing fracture plane, which occurred in L1T, did not occur in L3T. Comparing structural changes (Fig. 7) with flow (Fig. 8) reveals the formation of a high porosity zone in the matrix due to dissolution, with connection to the fracture plane. We speculate that narrow restrictions in the initially heterogeneous fracture plane may have trapped particulates during transport and diverted reactive flow into the surrounding matrix, similar to formation and development of wormholes through gel (Brattekås et al., 2017).

In cores with tight fractures (L4T and L5T) increased impedance factors were observed (permeability decreased post-dissolution), which suggests that reactive flow, and consequently dissolution, predominantly occurred outside of the fracture plane. Note the difference in calculated impedance factor (Table 4), resulting from the presence/absence of initial flow along the fracture edges. Compact conical dissolution was observed in both cores (figure A5). Additional development of small wormholes was observed in a fractured core sample with increased impedance factor of 1.5 (L5T, Fig. 9). The formation of wormholes across the cross-sectional area suggested that reactive flow

was not restricted to the fracture plane.

External structural changes, such as compact-conical dissolution at the inlet face, can be quantified by visual observations, but access to local changes in flow and structure within the opaque porous medium was only achieved by in-situ imaging. Post-dissolution visualization of structure and fluid flow properties in selected cores indicated that dissolution and precipitation reactions (and consequently impedance) were strongly affected by local heterogeneities in the fracture plane. Dissolution in the fracture plane was promoted in some cores (L1T), as expected. Dissolution in the adjacent matrix was, however, also observed in both open and tight fractures. It is likely that a locally decreased fracture conductivity, caused by secondary precipitation and trapped dissolved particles, promoted dissolution outside of the fracture plane; as observed by wormhole development (tight-fracture L5T) and dissolution adjacent to the fracture plane (open-fracture L3T). Reduced injectivity was, however, only observed for core L5T in global Darcy scale measurements. Wormhole development was only observed in one tight fracture core (L5T), but did not form in tight-fracture (L4T) or whole (L2) systems where co-injection was performed under similar
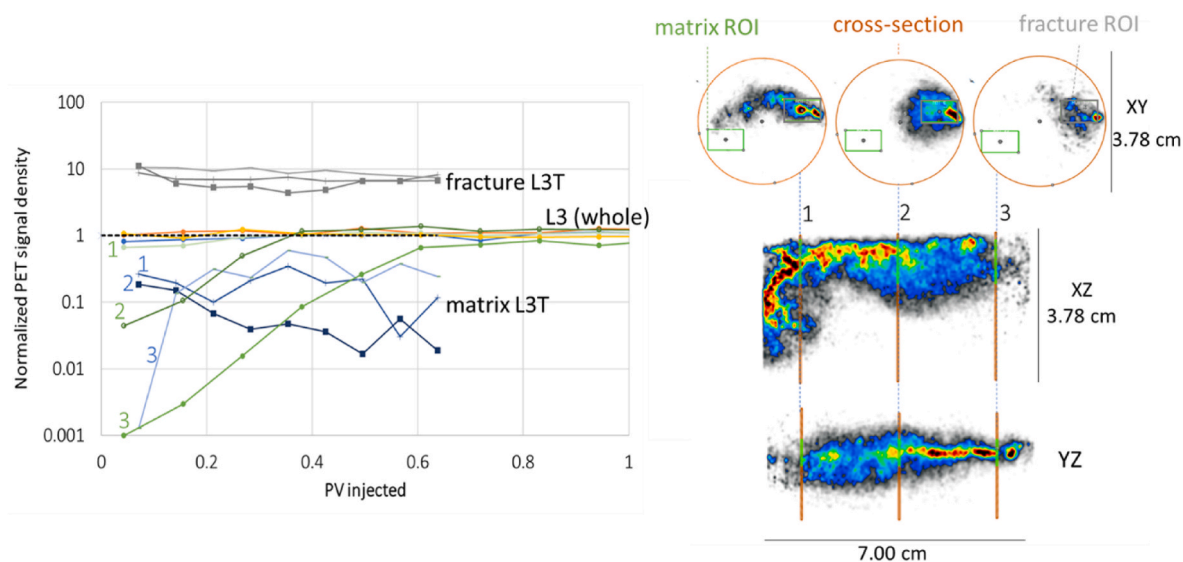
Fig. 8. Comparison of local flow paths in whole and fractured systems at three different positions along the core length (1, 2 and 3). <u>Left</u>: Development in local PET signal (labeling the brine) in whole (core L3) and fractured (core L3T) systems. The local PET signal is normalized to the XY-plane signal density (PET signal/volume) at each position. A piston-like displacement was observed in two small regions of interest (ROI) in L3, and both ROIs carried an equal volume of traced fluid (ROIs are indicated by small squares in the top <u>right</u> figure; both coincide with matrix in L3. In L3T the green square represents the matrix, and the grey represents the fracture). Traced water injection into L3T showed that flow occurred both within and outside of the pre-existing fracture plane: the signal in the fracture immediately increased upon injection of traced water. The signal in the matrix also increased to a maximum within 0.2 PV injected, although with a lower intensity. Our analysis shows that the L3T matrix conducts approximately 10% of flow, predominantly adjacent to the fracture plane.
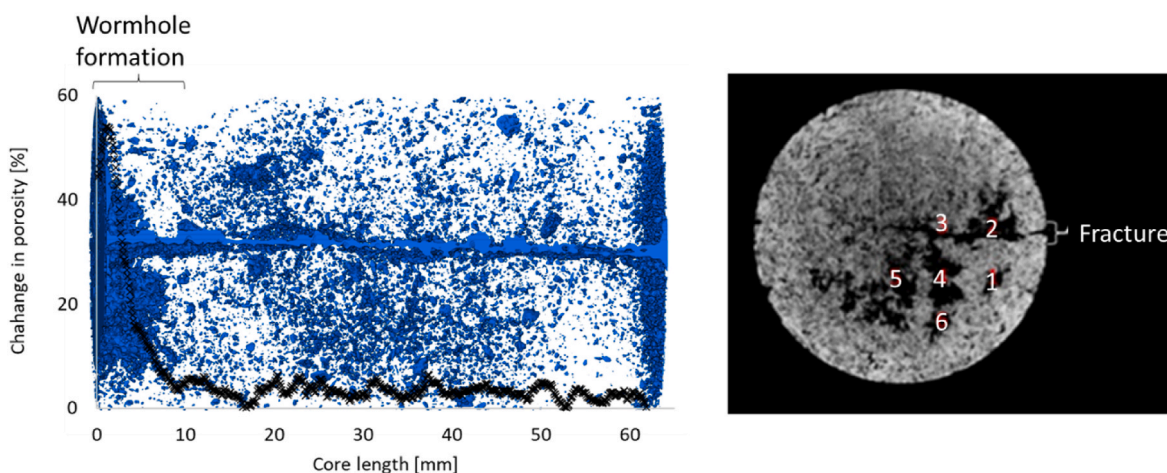
Fig. 9. Structural changes in rock structure in fractured core L5T after dissolution. <u>Left</u>: A 3D rendering of μCT images shows global dissolution (void >50 μm, blue), but predominantly at the end faces (inlet and outlet). Both compact-conical dissolution at the inlet and formation of multiple wormholes was observed. A porosity profile (showing the change from before and after co-injection, black) overlay the 3D image of the core porosity: up to 60% change in porosity was observed in the first 10 mm of the core, with minor changes (approximately 5%) in the remaining core. <u>Right</u>: 2D μCT image (XY-plane) close to the inlet (1.5 mm) showing the fracture plane and six wormholes. Smaller wormholes (1, 3–6) formed outside of the fracture plane, while the most prominent wormhole (2) extended 13.5 mm (20% of the core length) in proximity to the fracture. <u>Note</u>: The 2D XY μCT image was obtained 1.5 mm from the core inlet, where compact conical dissolution was not dominant. The reader is referred to supplementary material for additional images (Figure B4).

conditions.

3.3. Summarizing discussion

Dissolution of carbonate rock was observed in all studied systems during co-injection of supercritical CO_2 and water; and was confirmed by Darcy scale weight loss or effluent (calcite mineral production) measurements. Less than 2% of mass loss was recorded for the Edwards limestone rock material, during injection of 400 PV of CO_2 and brine. Injectivity development, accessed through dynamic pressure measurements, indicated two dissolution categories: *increasing* and *decreasing*.

Injectivity decreased in whole and tight-fracture cores, presumably due to flow obstruction (lodged or precipitated minerals), limiting the initial flow path. Open-fracture cores presumably confined reactive flow in the fracture plane and efficiently produced dissolved particles (i.e. increased injectivity). The differences in injectivity were determined based on pressure measurements, but other global measurements (e.g. the produced effluent pH development (Fig. 3)) corroborated the existence of the two distinct injectivity categories. Darcy-scale behavior, hence, indicated similar and distinct dissolution properties within for whole, tight fracture and open fracture cores, respectively.

Access to local flow (μPET) and structural changes (μCT), however,

showed that dissolution and precipitation reactions were strongly affected by local heterogeneities and inconsistent within the pre-defined categories. *In-situ* imaging confirmed different dissolution patterns and significantly localized (mm scale) effects: in whole cores dissolution occurred predominantly at the inlet (all cores). Cementation (L4) and high-porosity regions (L3) irregularly occurred in the core interior, while other cores (L2 and L7) did not undergo quantifiable structural changes during CO_2 and brine co-injection. In one tight-fracture core (LT5) developing wormholes were observed across the fracture plane. Dissolution in open-fracture cores was visualized within the fracture plane (L1T), as expected, but also both within and around the fracture plane (L3T). Local dissolution within the core interior, e.g. outside of the fracture plane was not detectable in Darcy scale measurements, but clearly influential on fluid flow, as captured by μPET.

Our work shows that dissolution of heterogeneous limestone rock material depends on local rock/fluid interactions and localized features of the core samples (e.g. irregular fracture apertures or PSD). Coupled with reactive flow, these features become determining factors for localized dissolution and developing flow patterns. Darcy scale measurements of heterogeneity and dynamic development during co-injection did not sufficiently capture the dissolution properties within the core samples. The inconsistency in developing flow patterns at this relatively small scale implies that field scale dissolution prediction is an utterly complex task in heterogeneous carbonate. Carbonates on larger scale will likely include most of the features investigated in this study: matrix with varying permeability and both tight and open fractures: where this work highlights the significant variation in dissolution patterns formed within each of these categories. Channeling in carbonates is clearly a dynamic issue; where displacement patterns may shift during reactive flow, depending on the degree and localization of dissolution. This has implications for larger scale channeling of CO_2: in fractured reservoirs, where the reservoir rock is reactive and prone to dissolution, channeling may worsen (continuous erosion of fracture to larger aperture as in L1T) or improve (dissolved particles lodging in irregular fracture aperture and diverting fluid flow as in L3T) with time. By comparing μPET and μCT we can confirm that PET is able to capture mm-scale changes within the porous matrix, such as cementation and dissolution. Recent work (Kurotori et al., 2023) also showed the potential of PET imaging to quantify fracture structure. Multi-modal imaging of dynamic reactive fluid displacements in different fracture systems is possible with the system used in this work, and would provide important information about the development of dissolution and displacement patterns in complex rocks. The experiments presented in this work clearly shows that imaging is an important asset in determining dissolution flow patterns; whereas Darcy scale measurements should be more carefully interpreted.

4. Conclusions

The worldwide abundance of carbonate formations and reservoirs makes storage of CO_2 in such formations highly likely. However, the reactive nature of carbonate minerals increases the importance of understanding dynamics and dissolution processes, which occur during CO_2 injection, to enable long term safe storage. Study of the relationship between carbonate dissolution and Darcy-scale structural changes in core plugs (under relevant storage conditions) with and without pre-existing highly permeable fractures have resulted in the following main conclusions:

- Darcy scale measurements confirmed calcite dissolution by co-injection of brine and CO_2 in Edwards limestone outcrop cores. Measurements included visual inspection of core exteriors, weight changes, effluent analysis (pH and precipitates) and differential pressure development.

- Injectivity *increased* during two-phase injection of CO_2 and brine in cores with open fractures. *In-situ* imaging confirmed localized dissolution in (L1T) or around (L3T) the fracture plane.
- Injectivity *decreased* during two-phase injection of CO_2 and brine in cores with tight fractures. *In-situ* imaging revealed that reactive flow occurred across the core cross-section, and dissolution was, hence, not restricted to the fracture plane. Compact conical dissolution and wormhole formation was observed.
- Injectivity *decreased* during two-phase injection of CO_2 and brine in whole cores. *In-situ* imaging identified cementation in the core matrix as a possible mechanism for injectivity reduction. The changes in structure (μCT) influenced core scale flow (μPET).

Author contribution

Conceptualization: Martin A. Fernø; and Bergit Brattekås; Methodology: Malin Haugen, Olav Parelius Folkvord, Torunn Veien, Martin A. Fernø; and Bergit Brattekås; Formal analysis: Malin Haugen, Olav Parelius Folkvord, Torunn Veien, Martin A. Fernø; and Bergit Brattekås; Investigation: Malin Haugen, Olav Parelius Folkvord, Torunn Veien and Bergit Brattekås; Writing: Malin Haugen, Olav Parelius Folkvord, Torunn Veien, Martin A. Fernø; and Bergit Brattekås; Visualization: Malin Haugen, Olav Parelius Folkvord, Torunn Veien, Martin A. Fernø; and Bergit Brattekås; Funding acquisition: Martin A. Fernø

Declaration of competing interest

The authors declare that they have no known competing financial interests or personal relationships that could have appeared to influence the work reported in this paper.

Data availability

Data will be made available on request.

Acknowledgements

Appendix A. Supplementary data

Supplementary data to this article can be found online at https://doi.org/10.1016/j.jgsce.2023.205139.

References

Alcorn, Z., Graue, A., Karakas, M., 2022. CO2 Foam Pilot in a Heterogeneous Carbonate Reservoir: Analysis and Results. https://doi.org/10.2118/209359-MS.

Al-Khulaifi, Y., et al., 2019. Pore-scale dissolution by CO2 saturated brine in a multimineral carbonate at reservoir conditions: impact of physical and chemical heterogeneity. Water Resour. Res. 55 (4), 3171–3193. https://doi.org/10.1029/2018WR024137.

Benson, S.M., Cole, D.R., 2008. CO₂ sequestration in deep sedimentary formations. Elements 4 (5), 325–331. https://doi.org/10.2113/gselements.4.5.325.

Brattekås, B., M, S., Graue, A., Fernø, M.A., Espedal, H., Seright, R.S., 2017. New insight into wormhole formation in polymer gel during water chase floods with positron emission tomography. SPE J. 22 (1) https://doi.org/10.2118/180051-PA.

Brattekås, B., et al., 2020. Foam flow and mobility control in natural fracture networks. Transport Porous Media 131 (1), 157–174. https://doi.org/10.1007/s11242-019-01249-3.

Brattekås, B., et al., 2023. Of rats and rocks: using pre-clinical PET imaging facilities in core analysis. E3S Web Conf. 366, 01011 https://doi.org/10.1051/e3sconf/202336601011.

Fernø, M.A., et al., 2015. Mobility control during CO2 EOR in fractured carbonates using foam: laboratory evaluation and numerical simulations. J. Petrol. Sci. Eng. 135, 442–451. https://doi.org/10.1016/j.petrol.2015.10.005.

Gaus, I., 2010. Role and impact of CO2–rock interactions during CO2 storage in sedimentary rocks. Int. J. Greenh. Gas Control 4 (1), 73–89. https://doi.org/10.1016/j.ijggc.2009.09.015.

Hommel, J., Coltman, E., Class, H., 2018. Porosity–permeability relations for evolving pore space: a review with a focus on (Bio-)geochemically altered porous media. Transport Porous Media 124 (2), 589–629. https://doi.org/10.1007/s11242-018-1086-2.

IPCC, 2005. Special Report on Carbon Dioxide Capture and Storage, pp. 195–276 (Chapter 5): Underground geological storage.

Kurotori, T., Zahasky, C., Gran, M., et al., 2023. Comparative analysis of imaging and measurements of micrometer-scale fracture aperture fields within a heterogeneous rock using PET and X-ray CT. Transport Porous Media 147, 519–539. https://doi.org/10.1007/s11242-023-01922-8.

Laboratory, N.E.T., 2010. Carbon Dioxide Enhanced Oil Recovery.

Larkin, R., Creel, P., 2008. Methodologies and solutions to remediate inter-well communication problems on the SACROC CO2 EOR project – a case study. In: SPE Symposium on Improved Oil Recovery. OnePetro, Tulsa, Oklahoma, USA. https://doi.org/10.2118/113305-MS.

Lemmon, E., McLinden, M., Friend, D., 2020. Thermophysical Properties of Fluid Systems.

Luhmann, A.J., et al., 2014. Experimental dissolution of dolomite by CO2-charged brine at 100°C and 150bar: evolution of porosity, permeability, and reactive surface area. Chem. Geol. 380, 145–160. https://doi.org/10.1016/j.chemgeo.2014.05.001.

Luquot, L., Gouze, P., 2009. Experimental determination of porosity and permeability changes induced by injection of CO 2 into carbonate rocks. Chem. Geol. 265 (1), 148–159. https://doi.org/10.1016/j.chemgeo.2009.03.028.

Maheshwari, P., et al., 2013. 3-D simulation and analysis of reactive dissolution and wormhole formation in carbonate rocks. Chem. Eng. Sci. 90, 258–274. https://doi.org/10.1016/j.ces.2012.12.032.

Minto, J.M., et al., 2017. X-ray CT and multiphase flow characterization of a 'bio-grouted' sandstone core: the effect of dissolution on seal longevity. Int. J. Greenh. Gas Control 64, 152–162. https://doi.org/10.1016/j.ijggc.2017.07.007.

Oelkers, E.H., Gislason, S.R., Matter, J., 2008. Mineral carbonation of CO_2. Elements 4 (5), 333–337. https://doi.org/10.2113/gselements.4.5.333.

Ott, H., Oedai, S., 2015. Wormhole formation and compact dissolution in single- and two-phase CO2-brine injections. Geophys. Res. Lett. 42 (7), 2270–2276. https://doi.org/10.1002/2015GL063582.

Smith, D.D., MJ, G., Kemp, C.C., McBee, M., Taitano, J.A., Winfield, M.S., Portwood, J.T., Everett, D.M., 2006. The successful evolution of anton Irish conformance efforts. In: SPE Annual Technical Conference and Exhibition. OnePetro, San Antonio, Texas, USA. https://doi.org/10.2118/103044-MS.

Smith, M.M., et al., 2013. CO2-induced dissolution of low permeability carbonates. Part I: characterization and experiments. Adv. Water Resour. 62, 370–387. https://doi.org/10.1016/j.advwatres.2013.09.008.

Tipura, L., 2008. Wettability Characterization by NMR T2 Measurements in Edwards Limestone. Bergen: Department of Physics and Technology, University of Bergen, Master Thesis.